**Proceedings of the ASME 2025 44th International
Conference on Ocean, Offshore and Arctic Engineering
OMAE2025
June 22-27, 2025, Vancouver, British Columbia, Canada**

OMAE2025-156362

WAVE INDUCED RESPONSE OF SHALLOW DRAFT INTERCONNECTED PONTOONS

William Otto
MARIN
Wageningen,
Netherlands

Thomas Kluwer
Oceans of Energy
Sassenheim,
Netherlands

Spyros Hirdaris
ABS
Athens,
Greece

ABSTRACT

This paper presents the wave induced responses of shallow draft interconnected pontoons as investigated by the EU-funded project BAMBOO. The project aims to tackle the barriers for the implementation of a sustainable, large-scale offshore solar farm of 1km^2/150 MW, that will act as a blueprint for the rollout of offshore solar projects in Europe.

Special focus is attributed to the influence of wave frequent horizontal motions and axial interconnector loads on such installations. It is shown that the horizontal motions and axial connector loads are mainly related to the array length to wavelength aspect ratio. For stiff connectors, the axial connector loads RAOs vary between zero and a value that is twice the cross-sectional weight. The axial loading pattern for lower axial stiffness values is similar to the stiff solution, whereas dynamic amplification occurs in way of axial vibration modes. An analytical solution is derived for the axial natural frequencies and loading patterns. It is shown that in head waves the horizontal motions are in good agreement with results from diffraction theory and model tests. It is also concluded that expanding an array by adding more pontoons will significantly reduce the wave frequent horizontal motions, which leads to lower variations in mooring line tensions.

Keywords: FPV, Offshore Solar

NOMENCLATURE

Symbol	Quantity
B	Width of pontoon
c	Axial connector stiffness
daf	Dynamic Amplification Factor
e	Euler’s number (*~2.71828*)
F	Force
F_{FK}	Froude-Krylov Force
g	Gravity constant
i	Imaginary number $(-1)^{0.5}$
k	Wave number $2\pi/\lambda$
L_a	Length of array
L_{pp}	Length of pontoon
m	Pontoon mass
N	Number of pontoons in length direction
p	Pressure
S	Power spectral density
Q_a	Modal force amplitude
q_a	Modal response amplitude
t	Time
T	Draft or Tension
U_n	Axial displacement mode shape n
u	Axial displacement
v	Eigen vector, mass normalized
x	Horizontal coordinate
z	Vertical coordinate
ζ_a	Wave amplitude
ζ_n	Modal damping ratio
λ	Wave length or eigenvalue
ρ	Water density
Φ	Phase angle
ω	Angular frequency

1. INTRODUCTION

In the years to come worldwide demand for energy is set to continuously rise [1]. Currently EU explores the potential of more sustainable options to meet emerging energy demands and review their energy sector strategies that aim to account for renewable energy production into the energy mix [2]. A noteworthy area is the development of hybrid offshore wind / solar parks. Offshore solar extends the potential of photovoltaics at enormous scales and can enable Europe to meet their climate neutral policies for 2030 and 2050 [3]. This is because it makes use of abundant space at sea, satisfies economies of scale and is a complementary energy yield. The latter could be supported by the development and certification of hybrid floating wind / floating solar farm installations that can enable the utilization of existing offshore cable infrastructures and provide stable energy output with low impact on marine ecosystems.

Since December 2023 Oceans of Energy leads the European Climate, Infrastructure and Environment Executive Agency (CINEA) sponsored BAMBOO (Build scAled Modular Bamboo-inspired Offshore sOlar systems) consortium with the aim to tackle the barriers for a sustainable, large-scale offshore Floating PhotoVoltaics (FPV) system of 1 km^2/150 MW. The scope of the project is to enable 1km^2/150 MW hybrid wind/offshore solar installations. One of the technical pieces of the puzzle is the hydrodynamic assessment of large-scale interconnected floating solar arrays. This paper focuses on how the floating offshore installation response changes while expanding the array to 1km^2/150 MW. Wave frequent horizontal motions and axial connector loads are assessed and compared. The results may be considered important for the development of future classification rules, design assessment procedures and the certification of hybrid wind solar farm installations.

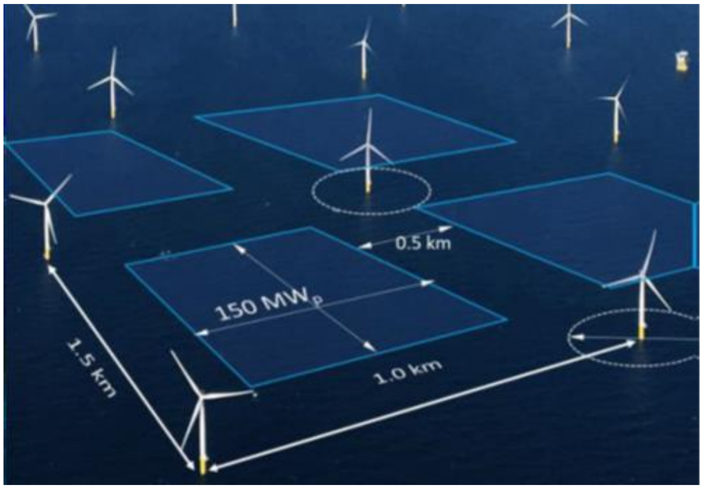

FIGURE 1: LARGE SCALE OFFSHORE FPV OF 1 KM^2/150 MW IN AN OFFSHORE WIND FARM

2. ANALYTICAL SOLUTION

An analytical solution has been derived for the wave frequent horizontal motions and axial connector loads. The main advantage of this analytical solution is that it could assist with our general understanding of the physical dynamic behavior of the floating installation under development. The disadvantage is that the solution is not that accurate due to several simplifications and assumptions. In the model presented the most important assumption is that the diffraction effect is small, i.e. the wave field leeward of the array is not significantly affected by the presence of the array system itself (see Section 3). The wave steepness is assumed to be small and therefore the dynamic behavior of the system is assumed linear. Under these assumptions, the wave excitation on a pontoon effectively becomes equivalent to the Froude-Krylov force which describes the integration of the undisturbed wave pressure over the wetted hull of the FPV.

2.1 Wave excitation on an array

The undisturbed wave pressure is described by the Airy wave solution. For deep water, this pressure can be simplified to [4]:

$$p = \rho g \zeta_a e^{kz} \sin(kx - \omega t) \tag{1}$$

The term e^{kz} implies that the wave pressure varies over the water column. The pontoons have a shallow draft. Thus, the wave pressure remains constant over the draft of the pontoon and approximately the same as the pressure in way of the free surface ($e^{kz} = 1$). In surge direction, F_{FK} on a pontoon is the difference between its bow and stern values. For a small pontoon L_{pp}, the pressure difference between bow and stern can be approximated by the formulae:

$$p_{bow} - p_{stern} = L_{pp} \left.\frac{dp}{dx}\right]_{cog} = \rho g \zeta_a \, k L_{pp} \, \cos(k x_{cog} - \omega t) \tag{2}$$

The F_{FK} on a single pontoon then becomes the pressure difference times the frontal area BT. The relation between array and wave length can be established using the expression :

$$kL_{pp} = \frac{2\pi}{\lambda}\frac{L_a}{N} = 2\pi \frac{L_a}{\lambda}\frac{1}{N}, \qquad x_1 = 0, \qquad x_N = L_a$$

The net Froude Krylov force $F_{FK,array}$ is given by the summation over all the pontoons :

$$F_{FK,array} = \rho g \zeta_a \, BT \, 2\pi \, \frac{L_a}{\lambda} \left\{ \cos(\omega t) \frac{1}{N} \sum_{n=1}^{N} \cos\left(2\pi n \frac{L_a}{\lambda}\right) + \sin(\omega t) \frac{1}{N} \sum_{n=1}^{N} \sin\left(2\pi n \frac{L_a}{\lambda}\right) \right\} \tag{3}$$

A demonstration of the above for $\lambda = L_a$, is depicted in Figure 2. The arrows indicate the horizontal component of F_{FK}. The rising pontoons experience a force in the direction of the wave propagation, while the descending pontoons are pulled in the opposite direction. For this example the net force on the array is zero.

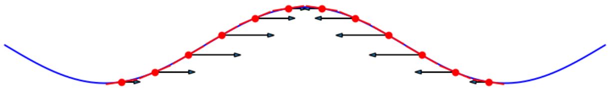

FIGURE 2: HORIZONTAL COMPONENT F_{FK} at $L_A/\lambda = 1.0$

When the amount of pontoons N is sufficiently large, we can replace the summation by the integral:

$$F_{FK,array} = \rho g \zeta_a \, BT \, 2\pi \, \frac{L_a}{\lambda} \left\{ \cos(\omega t) \frac{1}{{L_a}/{\lambda}} \int_0^{{L_a}/{\lambda}} \cos 2\pi \hat{x} \, d\hat{x} \right. \\ \left. + \ \sin(\omega t) \frac{1}{{L_a}/{\lambda}} \int_0^{{L_a}/{\lambda}} \sin 2\pi \hat{x} \, d\hat{x} \right\} \tag{4}$$

Solving the integrals and simplifying the result using goniometric functions gives:

$$F_{FK,array} = \rho g \zeta_a \, BT \ \sqrt{2 - 2\cos\left(2\pi \frac{L_a}{\lambda}\right)} \ \sin(\omega t + \phi_{FK}) \tag{5}$$

Under these assumptions, it turns out that the amplitude of the net wave excitation is a function of L_a/λ only,which expresses the ratio between an array length and a wavelength (see Figure 3).

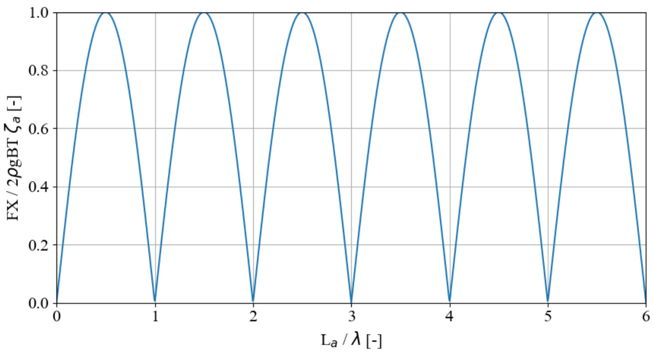

FIGURE 3: WAVE EXCITATION AMPLITUDE ON AN ARRAY

When the wavelength exactly fits within the array length, either a single time or an exact multitude, the force on the individual pontoons cancels out and the net force becomes zero (see Figure 2). In-between those cancellations, the net force RAO reaches a maximum value of twice the sectional weight ($Fx = 2 \rho g BT \zeta_a$).

2.2 Interpretation of wave excitation

Equation 5 indicates the Froude-Krylov force is only a function of the L_a/λ ratio. Neither the number of pontoons N nor the absolute array length L_a are included in this relationship. As this might be counterintuitive, Figure 4 illustrates three arrays with $L_a/\lambda = 1.5$. Figure 4 shows an array of 12 and 24 pontoons. The second array has twice the amount of pontoons, but the force on each pontoon is only half. Consequently, the net force amplitude on both arrays equals $2 \rho g BT \zeta_a$. As the wave pressure field (and gradient) underneath both arrays is the same, the force on each pontoon is proportional to L_{pp}. When N is large, the net force on the array becomes insensitive to the number of pontoons.

The absolute length of an array does not affect the force amplitude. For example, a 20m long array has the same force amplitude of $2 \rho g BT \zeta_a$ as a 200m long array. Figures 4 (a) and (c) respectively illustrate long and short arrays, both with $N = 12$ and both in a wave with ratio $L_a/\lambda = 1.5$. In (c), the pontoon length is only half but as the wave pressure gradient is double, the force is the same. Shorter waves comprise of water particles with higher accelerations, and hence a higher pressure gradient. The effect of a pontoon length and pressure gradient are cancelling out the effect of absolute length. Thus, L_a/λ appears to be more important for the force amplitude. The absolute array length is less relevant.

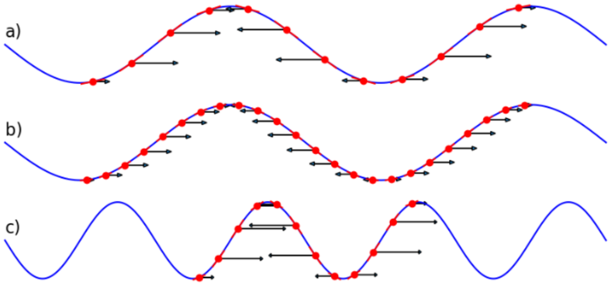

FIGURE 4: $L_a/\lambda = 1.5$, a) N = 12, b) N = 24, c) N = 12

Although the force amplitude of both arrays displayed in Figures 4 (a) and (c) is $2 \rho g BT \zeta_a$, array (a) is still likely to experience a larger absolute force. This is because depending on the site specific metocean data, the wave amplitude ζ_a of the longer wave can be significantly larger than the amplitude of the shorter wave.

2.3 Array horizontal motion response

We assume the mooring does not significantly influence the wave frequent motions of the array i.e., the mooring stiffness is low. Since the wave field leeward of the array is not significantly disturbed by the presence of the array, the wave radiation is also small and therefore the added mass and damping can be ignored. In Section 3 we will reflect on these assumptions and their consequences. The equation of motion in the horizontal plane simplifies to:

$$F_{FK,array} = m\ddot{x} = \rho \, L_a BT \, \ddot{x} \tag{6}$$

Double integration of Equations (5) and (6) over time twice gives:

$$x = \frac{1}{\omega^2} \frac{g}{L_a} \sqrt{2 - 2\cos\left(2\pi \frac{L_a}{\lambda}\right)} \ \zeta_a \sin(\omega t + \phi_x) \tag{7}$$

For deep water dispersion [4]:

$$\omega^2 = 2\pi \frac{g}{\lambda} \tag{8}$$

Thus,

$$x = \frac{1}{2\pi}\frac{\lambda}{L_a}\sqrt{2 - 2\cos\left(2\pi\frac{L_a}{\lambda}\right)}\;\zeta_a \sin(\omega t + \phi_x) \tag{9}$$

The RAO then becomes (see Figure 5):

$$RAO\ x = \frac{1}{2\pi}\frac{\lambda}{L_a}\sqrt{2 - 2\cos\left(2\pi\frac{L_a}{\lambda}\right)} \tag{10}$$

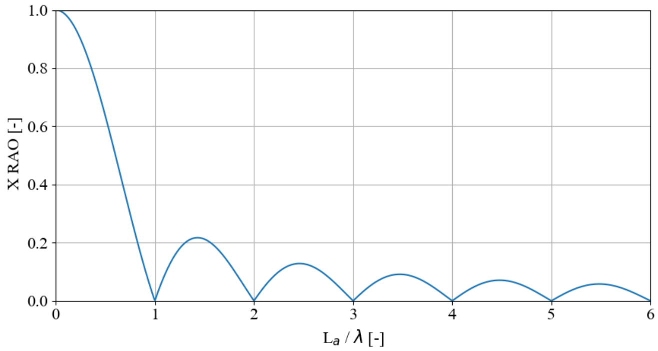

FIGURE 5: RAO HORIZONTAL MOTION

The pattern of the wave excitation is clearly visible, going to zero at the integer values and reaching a local maximum around 1.5, 2.5, 3.5, etc. In this figure, moving to the right means elongating the array, and adding more inertia to the system leads to a decreased response. For small arrays, in the limit of L_a towards zero, the inertia and the wave excitation both go to zero. They decrease at a rate such that the response reaches the asymptote of 1, meaning the array effectively behaves as a water particle.

The spectral density of the motion response in an irregular sea state is [5]:

$$S_x = S_\zeta \cdot RAO^2 \tag{11}$$

The significant value of the motion response becomes [5]:

$$X_{sign} = 4\sqrt{\int_0^\infty S_x d\omega} \tag{12}$$

Figure 6 shows the significant response as function of the array length for different peak period T_p values. On the top axis electrical power is presented as a reference, assuming a square array with 150 Watt/m². Increasing the array size decreases the wave frequent horizontal motions significantly. Expanding a small array towards 150 MW will significantly reduce the horizontal motions, and therefore also the mooring line tension variations associated to those.

The benefit of this derivation is that there is no CPU cost to construct this figure, and that there is no information required on the pontoon length, draft, width or connectors.

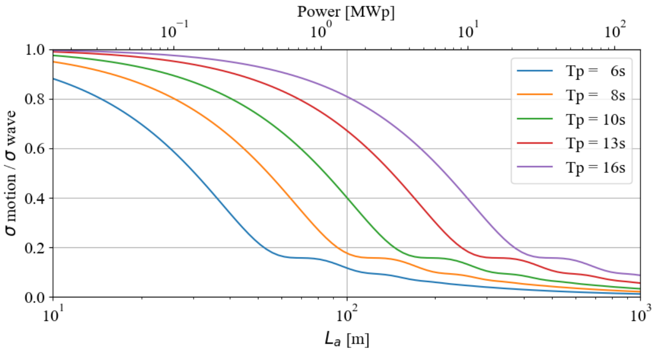

FIGURE 6: SIGNIFICANT MOTION RESPONSE FOR Hs = 1m, JONSWAP WAVE SPECTRUM WITH γ = 3.3

2.3 Axial flexible response with discrete masses

The axial loads and flexible responses are calculated with a linear combination of orthonormal modes. For a six-body system, this is shown in Figure 7.

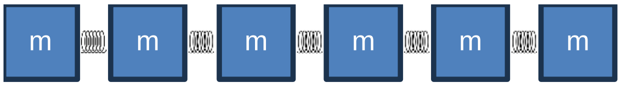

FIGURE 7: SIX BODY MASS SPRING SYSTEM

Assuming that each pontoon has a mass m and each connector has an axial stiffness c, the equation of motion for this system is:

$$\left[\begin{bmatrix} c & -c & & & & \\ -c & 2c & -c & & & \\ & -c & 2c & -c & & \\ & & -c & 2c & -c & \\ & & & -c & 2c & -c \\ & & & & -c & c \end{bmatrix} - \omega^2 \begin{bmatrix} m & & & & & \\ & m & & & & \\ & & m & & & \\ & & & m & & \\ & & & & m & \\ & & & & & m \end{bmatrix}\right]\begin{bmatrix} x_1 \\ x_2 \\ x_3 \\ x_4 \\ x_5 \\ x_6 \end{bmatrix} = \begin{bmatrix} F_1 \\ F_2 \\ F_3 \\ F_4 \\ F_5 \\ F_6 \end{bmatrix} \tag{13}$$

Where m includes the structural and added mass. The natural frequencies and associated mode shapes can be found by setting the external forcing to zero and divide the lefthand side by m:

$$\left\{\begin{bmatrix} c & -c & & & & \\ -c & 2c & -c & & & \\ & -c & 2c & -c & & \\ & & -c & 2c & -c & \\ & & & -c & 2c & -c \\ & & & & -c & c \end{bmatrix}\Big/ m - \lambda\, I\right\}\begin{bmatrix} x_1 \\ x_2 \\ x_3 \\ x_4 \\ x_5 \\ x_6 \end{bmatrix} = 0 \tag{14}$$

where I represents the identity matrix and λ an eigenvalue (not wave length), such that $\omega_n^2 = \lambda$. The eigenvalues and eigenvectors can solved only numerically. The eigenvectors v are mass normalized such that:

$$v^T m\, v \;= 1 \tag{15}$$

As an example, Figure 8 shows the 6 mass orthonormal mode shapes:

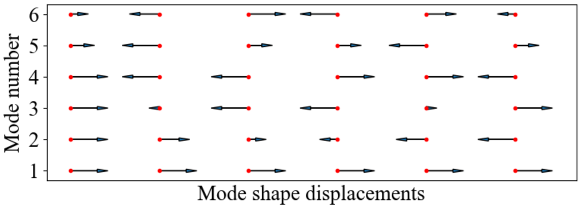

FIGURE 8: AXIAL MODE SHAPES FOR A 6 BODY SYSTEM

To calculate the excitation of each mode shape, we first rewrite the excitation amplitude $F_{FK,a}$ on a single pontoon as:

$$F_{FK,a}(\omega) = \rho g \zeta_a\, BT\;\; kL_{pp}\left(\cos\left(kx_{cog}\right) + i\;\sin\left(kx_{cog}\right)\right) \tag{16}$$

The real and imaginary parts of the amplitude are respectively in- and out of-phase with respect to the incoming waves. The excitation amplitude Q_a corresponding to each normal mode shape v is:

$$Q_a(\omega) = \rho g\; \zeta_a\; BT\;\;\; kL_{pp}\left\{\sum_{n=1}^{N} \mathrm{v}_n \cos(kx_n) + i\sum_{n=1}^{N} \mathrm{v}_n\; \sin(kx_n)\right\} \tag{17}$$

The modal force amplitude is a function of the wave number k. Figure 9 shows this wave excitation for the first 6 modes. Mode 1 corresponds to the surge excitation (see Figure 3). A similar cancellation pattern is evident in the higher mode shapes, with the odd and even numbered mode shapes shifted by 0.5 L / λ.

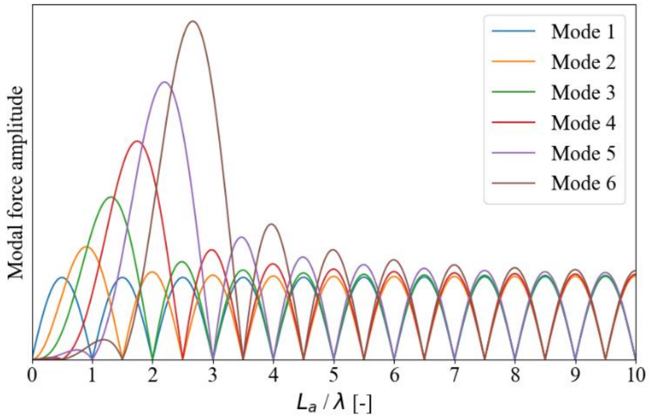

FIGURE 9: MODAL FORCE AMPLITUDE DISCRETE MASSES

The motion response amplitude for each normal mode shape becomes:

$$q_a = \frac{|Q_a|}{{\omega_n}^2} \frac{1}{\sqrt{\left(1-\left(\frac{\omega}{\omega_n}\right)^2\right)^2 + \left(2\zeta_n \frac{\omega}{\omega_n}\right)^2}} \tag{18}$$

As the mode shapes are orthogonal, the total motion of the pontoons can be obtained as a sum of the response for all mode shapes. It is important to take the phasing of each modal response into account. For each modal response, the phase angle between wave and motion is the summation of the angle between wave and modal forces and the angle between the modal force and the response:

$$\phi_{wave-\,motion} = \mathrm{atan2}(\Re\, Q, \Im\, Q) + \mathrm{atan2}\left(2\zeta_n \frac{\omega}{\omega_n}, 1 - \left(\frac{\omega}{\omega_n}\right)^2\right)$$

(19

Figure 10 shows the horizontal motion RAO and axial connector loads for an array comprising of 100 pontoons where the axial connector stiffness is high. When the number of pontoons is sufficiently large, this figure becomes insensitive to the number of pontoons. Straight vertical contour lines in the motion RAO indicate that all pontoons move together, i.e. the relative motions are small as the connectors are stiff. The surge induced RAO is effectively the same as the one depicted in Figure 5. The connector loads are varying between zero and $2\rho g BT\, \zeta_a$ while B should be interpreted as the average span between two connectors. For small arrays, $L_a / \lambda << 1$, the axial connector load tends to zero. Expanding the array increases the axial load till $L / \lambda = 1$, with the highest axial load in the array centre. Expanding the array does not lead to a higher axial connector load. The number of local maxima is equal to the L_a / λ value.

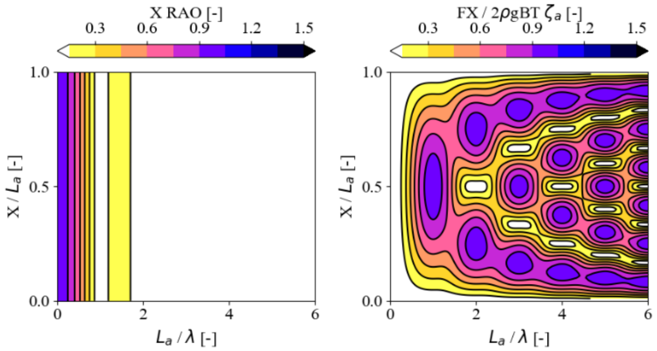

FIGURE 10: MOTION RAO (LEFT) AND AXIAL LOAD RAO (RIGHT), STIFF CONNECTORS

In Figure 11 the axial stiffness of the connectors is reduced, and chosen such that the natural frequency of the first mode corresponds to the wave frequency at $L / \lambda = 3$. The contour lines of the motion RAO are curved, indicating that there is relative motion between the pontoons. The leeward and waveward pontoons show more wave frequent movement than the central pontoons. The axial loading pattern is similar to the stiff solution yet it appears skewed and with some dynamic amplification.

The solution is particularly sensitive to 0.1 modal damping ratio. Damping comprises of two sources namely hydrodynamics and the mechanical damping of the connectors. Figures 12 and 13 show the solution for a damping ratio of 0.3 and 0.5 respectively.

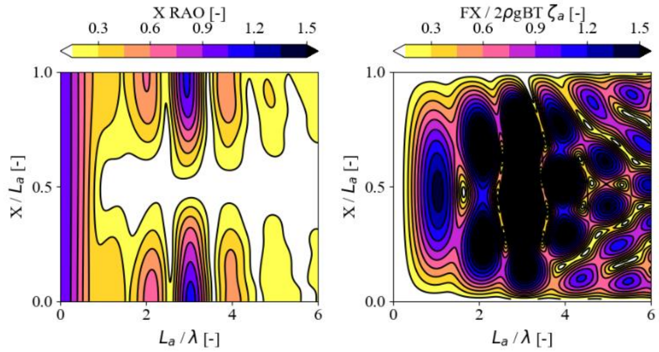

FIGURE 11: MOTION RAO AND AXIAL LOAD RAO, SOFT CONNECTORS, DAMPING RATIO 0.1

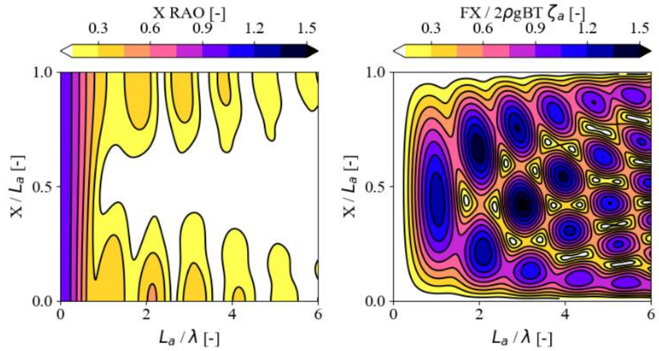

FIGURE 12: MOTION RAO AND AXIAL LOAD RAO, SOFT CONNECTORS, DAMPING RATIO 0.3

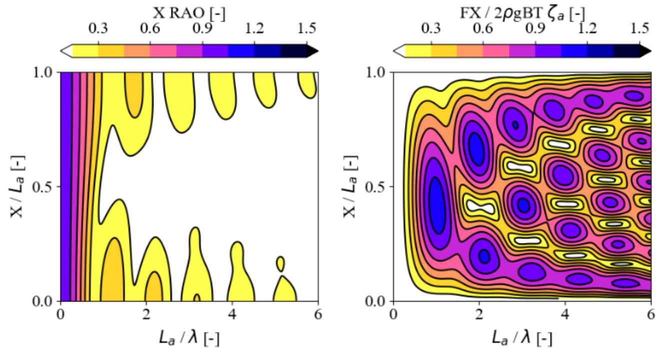

FIGURE 13: MOTION RAO AND AXIAL LOAD RAO, SOFT CONNECTORS, DAMPING RATIO 0.5

It is difficult to reduce connector loads by reducing axial stiffness. If the damping is high, the axial connector load can be reduced leading to reduced stiffness in way of the relative pontoon motions. Practically, collisions between pontoons should be avoided, and hence the relative motions should always be smaller than the gap size. As typically wave heights are an order of magnitude larger than the gap size, it is questionable whether the allowable relative motions are sufficient. The connector load can be reduced by adding damping. In this example the modal damping ratio has been chosen the same for each mode number.

2.3 Axial flexible response with continuous mass

The discrete mass approach presented in Section 2.2 can be used to investigate the influence of the number of pontoons. Above ~50 pontoons, the results displayed in Figures 13 to 16 converge. The larger the number of pontoons the more uniform the dynamic behavior of the array becomes, i.e. it behaves as a continuous rod with distributed mass and distributed axial stiffness (see Figure 14).

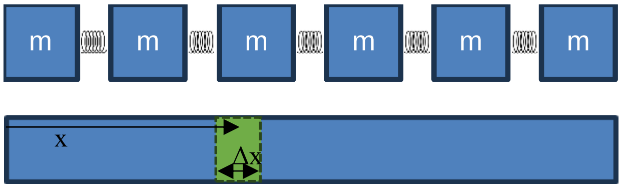

FIGURE 14: ARRAY REPRESENTED BY A CONTINUOUS ROD WITH AXIAL FLEXIBILITY

For such system the axial displacement *u* of a discrete element *Δx* is expressed by the following equation of motion [6] :

$$\frac{F(x,t)}{\Delta x} = EA\frac{\partial^2 u}{\partial x^2}(x,t) - \rho A\frac{\partial^2 u}{\partial t^2}(x,t) \tag{20}$$

The general solution to the above differential equation is $u(x,t) = U(x)T(t)$. If we assume orthogonal mode shapes:

$$u(x,t) = \sum_{n=1}^{\infty} U_n(x)T_n(t) \tag{21}$$

where U_n is mode shape number n. If we assume the waveward and leeward ends are free the mode shapes are expressed as:

$$U_n = C_n \cos\frac{n\pi x}{L} \tag{22}$$

Where C_n can be used to mass normalize the mode shapes:

$$\rho BT \int_0^L \left(C_n \cos\frac{n\pi x}{L}\right)^2 dx = 1 \tag{23}$$

Therefore:

$$C_n = \sqrt{\frac{1}{\rho\ \mathrm{BT} \int_0^L \cos^2\frac{n\pi x}{L}dx}} = \sqrt{\frac{2}{\rho\ \mathrm{LBT}}} \tag{24}$$

and the natural frequencies are expressed as:

$$\omega_n{}^2 = \left(\frac{n\pi}{L}\right)^2 \frac{EA}{\rho A} \tag{25}$$

The amplitude of F_{FK} for an increment Δx is:

$$F_{FK}(\omega) = \rho g \zeta_a \, BT \;\; k \, \Delta x \, (\cos kx + i \; \sin kx) \tag{26}$$

Hence, the modal force amplitude becomes:

$$\begin{aligned} Q_a(\omega) &= \int_0^L U_n F_{FK} dx \\ &= \rho g \zeta_a \, BT \;\; k \;\; C_n \left\{ \int_0^L \cos \frac{n\pi x}{L} \cos kx \, dx \right. \\ &\quad \left. + \, i \int_0^L \cos \frac{n\pi x}{L} \sin kx \, dx \right\} \end{aligned} \tag{27}$$

Solving the integrals gives:

$$\begin{aligned} &Q_a(\omega) \\ &= \; \rho g \zeta_a \, BT \;\; k \, C_n \, L \left\{ \frac{kL \cos n\pi \sin kL \; - n\pi \sin n\pi \cos kL}{k^2L^2 - \pi^2 n^2} \right. \\ &+ i \; \left. \frac{kL \cos n\pi \cos kL + n\pi \sin n\pi \sin kL - kL}{\pi^2 n^2 - k^2 L^2} \right\} \end{aligned} \tag{28}$$

As the mode shape number *n* is an integer, all terms with *sin(nπ)* are always zero and all terms with *cos(nπ)* are either 1 or -1, depending on whether *n* is even or odd. This greatly simplifies the equation to the format:

$$\begin{aligned} Q_a(\omega) = \; \rho g \zeta_a \, BT \;\; C_n \left\{ \frac{(kL)^2}{(kL)^2 - (n\pi)^2} \right\} \\ \{(-1)^n (\sin kL + i \; \cos kL) - i\} \end{aligned} \tag{29}$$

A solution is depicted in Figure 15.

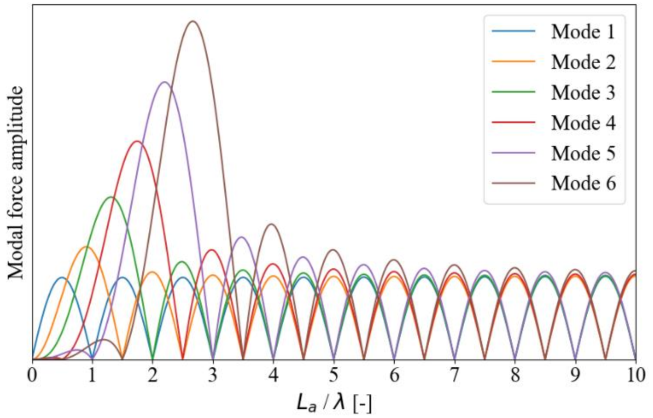

FIGURE 15: MODAL FORCE CONTINUOUS ROD

Note the similarities to Figure 9, i.e. the analytical solution for the continuous rod gives similar results as the numerical solution with discrete masses.

The motion response amplitude of each mode shape is defined as:

$$q_a = \frac{|Q_a|}{\omega_n{}^2} \frac{1}{\sqrt{\left(1 - \left(\frac{\omega}{\omega_n}\right)^2\right)^2 + \left(2\zeta_n \frac{\omega}{\omega_n}\right)^2}} \tag{30}$$

In the above equation the first ratio represents the quasi-steady response and the second the so called Dynamic Amplification Factor (DAF). For a uniform rod, the standard solution for the natural frequencies is:

$$\omega_n{}^2 = \left(\frac{n\pi}{L}\right)^2 \frac{EA}{\rho A} \tag{31}$$

We can translate this to the interconnected pontoons by considering that the axial stiffness of the full-length rod is:

$$c_{rod} = \frac{EA}{L} \tag{32}$$

In practice, the axial stiffness of the full-length array is the combination of all connectors in series. As there are *N-1* connectors for *N* pontoons, the equivalent axial stiffness of the array becomes:

$$c_{array} = \frac{c}{N-1} = \frac{EA}{L} \tag{33}$$

where *c* is the axial stiffness of 1 connector. The equivalence of EA of the rod then becomes:

$$EA = \frac{c \, L}{N-1} \tag{34}$$

For the sectional inertia *ρA* we this simplifies to *ρBT*. The omission of the added mass term is discussed in Section 3. The natural frequencies of the array therefore become:

$$\omega_n{}^2 = \frac{n^2 \pi^2 \, c}{\rho \, LBT \, (N-1)} \tag{35}$$

With this natural frequency, the quasi-steady response of equation (37) becomes:

$$\begin{aligned} \frac{|Q_a|}{\omega_n{}^2} = \frac{(\rho \, BT)^2 \, (N-1)}{n^2 \pi^2 \, c} \, gL \, \zeta_a \, C_n \left\{ \frac{(kL)^2}{(kL)^2 - (n\pi)^2} \right\} \\ \{(-1)^n (\sin kL + i \; \cos kL) - i\} \end{aligned} \tag{36}$$

Therefore, the axial displacement is expressed as:

$$u = \sum_{n=1}^{\infty} U_n q_a = \sum_{n=1}^{\infty} \frac{(N-1)}{n^2\pi^2\, c} (\rho\, BT)^2 g\, L\, \zeta_a\, {C_n}^2 \cos\frac{n\pi x}{L} \cdot \left\{\frac{(kL)^2}{(kL)^2-(n\pi)^2}\right\}\{(-1)^n(\sin kL + i\, \cos kL) - i\} \cdot daf \tag{37}$$

Using the established relation for C_n and following mass-normalization, this simplifies to:

$$u = 2\, \rho g\, BT\, \frac{(N-1)}{c} \zeta_a \sum_{n=1}^{\infty} \frac{1}{n^2\pi^2} \cos\frac{n\pi x}{L} \cdot \left\{\frac{(kL)^2}{(kL)^2-(n\pi)^2}\right\}\{(-1)^n(\sin kL + i\, \cos kL) - i\} \cdot daf \tag{38}$$

The force in way the connectors corresponds to the dynamic behavior of a rod in tension, i.e. Equation 24 applies leading to the expression:

$$T = -2\, \rho g\, BT\, \zeta_a \sum_{n=1}^{\infty} \frac{1}{n\pi} \sin\frac{n\pi x}{L} \cdot \left\{\frac{(kL)^2}{(kL)^2-(n\pi)^2}\right\}\{(-1)^n(\sin kL + i\, \cos kL) - i\} \cdot daf \tag{39}$$

Definition of the DAF requires knowledge of the ratio between wave and natural frequencies. By assuming deep water dispersion, we obtain:

$$\left(\frac{\omega}{\omega_n}\right)^2 = \frac{L}{\lambda} \frac{2\rho g BT\,(N-1)}{\pi\, n^2\, c} \tag{40}$$

For stiff connectors, DAF = 1 (see Figure 16). This is similar to Figure 10, i.e. when N is large, the analytical continuous rod idealization appears to be consistent with the numerically solved discrete mass approach.

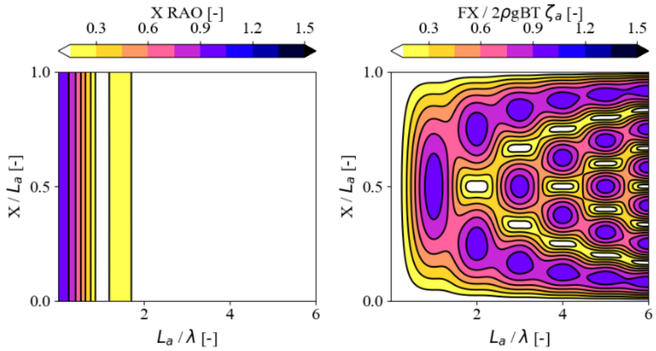

FIGURE 16: MOTION RAO (LEFT) AND AXIAL LOAD RAO (RIGHT), STIFF CONNECTORS

In Figure 17 the axial stiffness is chosen such that the natural frequency of the first elastic mode corresponds with the wave frequency at $L / \lambda = 3$. Hence, the stiffness is chosen so that:

$$c = 3 \cdot \frac{2\rho g BT(N-1)}{\pi} \tag{41}$$

Comparison of Figures 17 and 11 suggests that also for a non-stiff system the analytical solution is similar to the numerical solution. From this analytical solution we prove that the axial load in the connectors goes to exactly $2\rho g BT\, \zeta_a$ when the axial stiffness is high (DAF=1). For lower stiffness values, the dynamic amplification factor and hence the modal damping determines whether there is an increase or decrease in axial load.

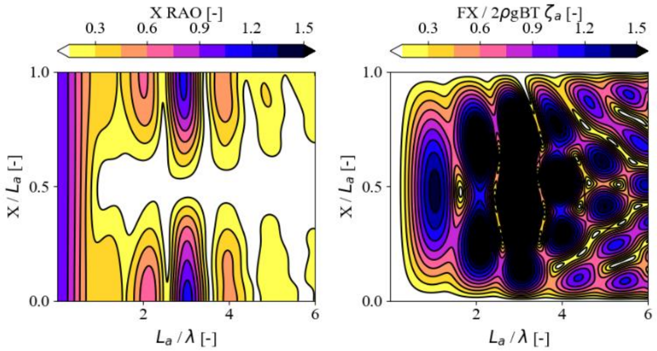

FIGURE 17: MOTION RAO AND AXIAL LOAD RAO, SOFT CONNECTORS, DAMPING RATIO 0.1

3. CASE STUDY WITH A LINEAR POTENTIAL FLOW METHOD

To study the influence of array size on the wave induced dynamics, diffraction hydrodynamics have been studied using software DIFFRAC [8]. This solver assumes an empirical correction for non-viscous flow and small wave amplitudes. It considers diffraction and radiation by means of a frequency domain Green function method [7].

3.1 Case description

Arrays have been designed for the sole purpose of studying the effect of the array length L, the amount of pontoons N and the pontoon length L_{pp}. The main characteristics are listed in Table 1. The dimensions of these arrays are chosen such that they can be tested in MARIN's Concept Basin at relevant L / λ ratios. Two pontoons were designed and herby designated as 'small' and 'large'. Note that 2 small pontoons, including 1 gap, have the same length as 1 large pontoon. Hence, an array of 6 large pontoons (including 5 gaps) has the same length as 12 small pontoons (including 11 gaps) while both arrays are 3.5m long. In this case study all arrays are 1 pontoon wide (1.00m)

Table 1: Case description pontoons

	L_{pp}	B	T	gap	Mass
Pontoon	[m]	[m]	[m]	[m]	[kg]
Large	0.5667	1.00	0.0239	0.02	13.85
Small	0.2733	1.00	0.0239	0.02	6.68

3.2 Wave frequent horizontal motions

To verify the surge motion RAO, the connectors between pontoons were at first considered to behave as hinges with linear spring behavior. A hinge can be modelled by choosing a high stiffness values in axial and shear directions while setting the rotational stiffness to zero. To practically determine what *'a high stiffness value'* is, the stiffness should be increased in steps. While increasing the stiffness, the relative motions reduce. Herewith the stiffness was increased till the relative motion RAOs < 0.01. Practical experience suggest that a further increase of the stiffness may eventually lead to numerical inaccuracies and therefore this is not recommended.

The shortest array had *N* = 6 pontoons expanded to 12, 24 and 48. The surge RAOs are plotted in Figures 18 and 19, for arrays consisting of small and large pontoons respectively. All arrays follow the trends of the analytical solution very well. The longer arrays are closer to the analytical solution than the shorter ones. DIFFRAC takes the added mass into account, while the analytical solution assumed this is almost negligible. This comparison suggests that the added mass inclusion does not influence the surge RAO.

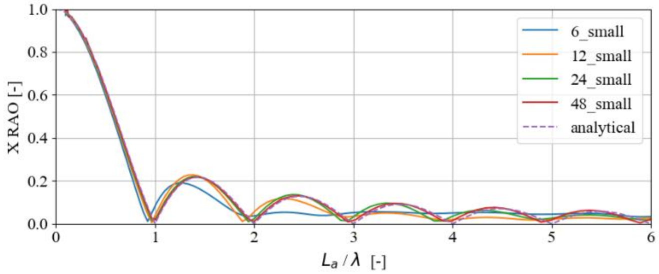

FIGURE 18: SURGE RAO SMALL PONTOONS DIFFRAC

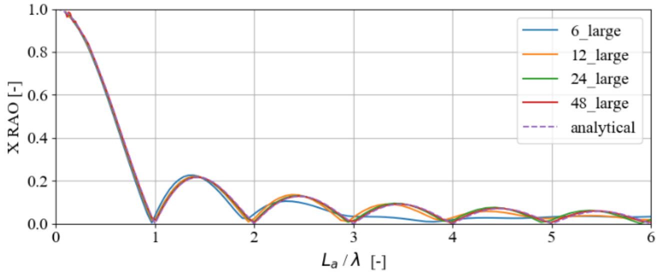

FIGURE 19: SURGE RAO LARGE PONTOONS DIFFRAC

3.3 Wave frequent axial loads – stiff hinges

Using the high axial stiffness from Section 3.2, the axial load RAO from DIFFRAC is plotted in Figures 20 and 21, for arrays consisting of small and large pontoons respectively. One trivial reason why the analytical solutions start to deviate from DIFFRAC is that the individual pontoons are not short as compared to the wave. Note that in the analytical solution we assume a constant pressure gradient over the length of an individual pontoon (see Equation 2). When the pontoon length reaches the same order of magnitude as the wave length, this is no longer the case. The second reason why the analytical solution deviates can be attributed to the influence of radiation and diffraction.

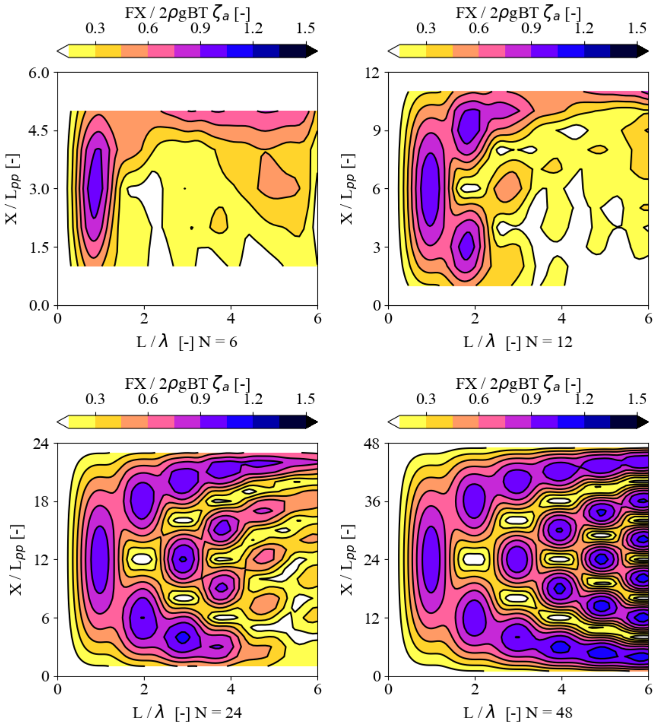

FIGURE 20: AXIAL LOAD RAO SMALL PONTOONS, N = 6 (TOP LEFT) TO N = 48 (BOTTOM RIGHT)

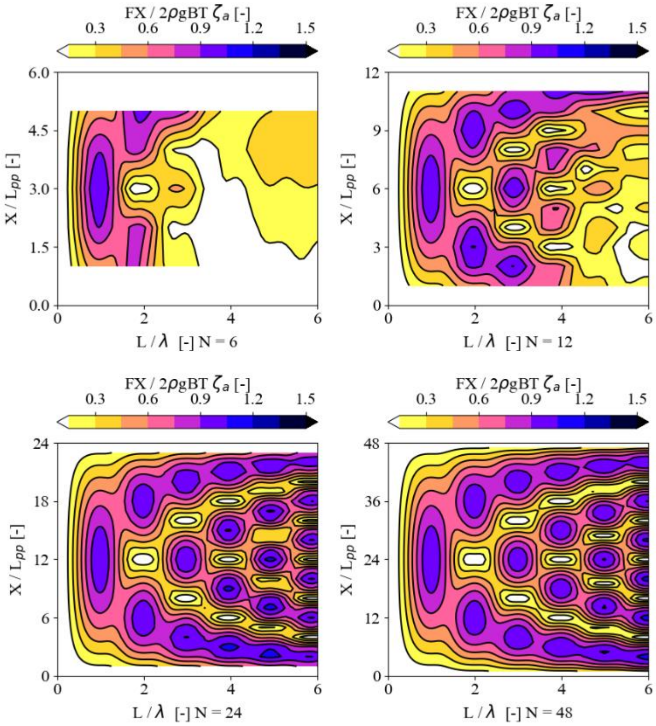

FIGURE 21: AXIAL LOAD RAO LARGE PONTOONS, FROM N = 6 (TOP LEFT) TO N = 48 (BOTTOM RIGHT)

3.4 Wave frequent axial loads – soft hinges

The influence of axial connector stiffness has been investigated in DIFFRAC using the 24 large array. Four different stiffness values have been chosen such that the analytically derived natural frequency of the first mode corresponds to the wave frequencies at $L / \lambda = 2,3,4$ and 5.

Table 2: First axial mode, stiffness variation

C	ωₙ at L / λ	Analytic dry ωₙ	Diffrac dry ωₙ	Diffrac wet ωₙ	Radiation Damping	Ca
[N/m]	[-]	[rad/s]	[rad/s]	[rad/s]	[-]	[-]
7.02E3	2	2.96	2.95	2.89	0.0003	0.042
1.05E4	3	3.63	3.61	3.53	0.0004	0.043
1.41E4	4	4.19	4.17	4.08	0.0005	0.043
1.76E4	5	4.68	4.67	4.56	0.0007	0.043

As described in Table 2 for all cases the dry natural frequency of DIFFRAC is within 0.5% of the analytical solution. The added mass for the first natural mode in this case is 4% of the dry mass, which explains why the analytical solution is a good estimate. The added mass is not frequency dependent in the tested range. The radiation damping considered is less than 1% of the critical damping. It is noted that the hydrodynamic damping will also have a viscous component. The solution of those 4 cases, including a modal damping ratio of 0.1 (assumed to be from the connectors), is shown in Figure 22.

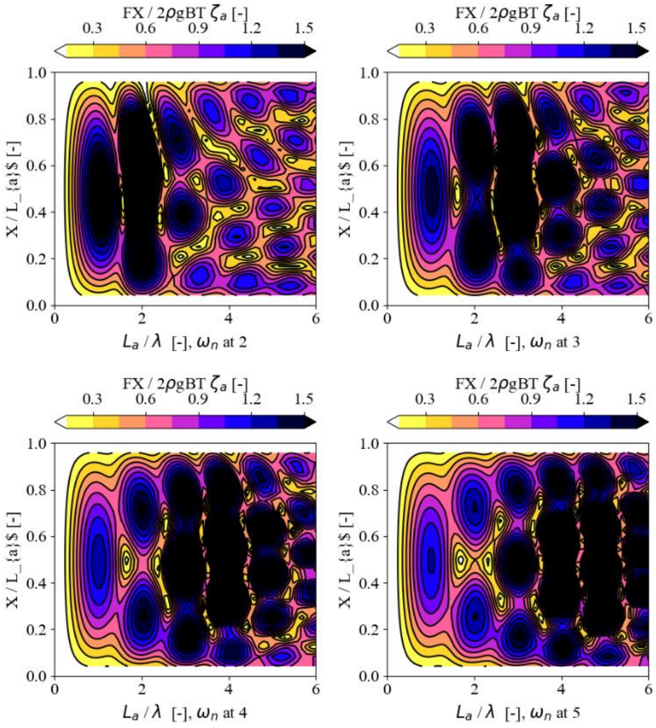

FIGURE 22: AXIAL LOAD RAO LARGE PONTOONS, N=24, FROM ωN AT 2 (TOP LEFT) TO ωN AT 5 (BOTTOM RIGHT)

The variation in the number of pontoons shown in Table 3 and Table 4 respectively corresponding to the small and large pontoons. The magnitude of the added mass results from gap dynamics and hence the number of pontoons per gap *N/(N-1)* is an important parameter. The added mass coefficient is plotted against this ratio in Figure 23, which shows a clear linear relation between the amount pontoons per gap and the added mass. When the number of pontoons is large, i.e. *N/(N-1)* = 1, the large pontoons have an added mass of 3% and the small pontoons an added mass of 6%. These percentages are probably dependent on the pontoon gap to T and L_{pp} ratios. However, this matter is under further investigation.

Table 3: First axial mode, variation in N small pontoons

N	c	Analytical dry ωₙ	Diffrac dry ωₙ	Diffrac wet ωₙ	Radiation Damping	Ca
[-]	[N/m]	[rad/s]	[rad/s]	[rad/s]	[-]	[-]
6	2290	10.31	9.58	8.83	0.0223	0.179
8	3206	8.91	8.55	7.98	0.0154	0.147
12	5038	7.27	7.17	6.79	0.0076	0.116
24	10534	5.13	5.19	4.97	0.0017	0.087
48	21527	3.63	3.72	3.59	0.0004	0.074

Table 4: First axial mode, variation in N large pontoons

N	c	Analytical dry ωₙ	Diffrac dry ωₙ	Diffrac wet ωₙ	Radiation Damping	Ca
[-]	[N/m]	[rad/s]	[rad/s]	[rad/s]	[-]	[-]
6	2290	7.27	6.66	6.36	0.0070	0.096
8	3206	6.29	5.94	5.72	0.0040	0.076
12	5038	5.13	4.98	4.84	0.0017	0.058
24	10534	3.63	3.61	3.53	0.0004	0.043
48	21527	2.56	2.58	2.54	0.0001	0.036

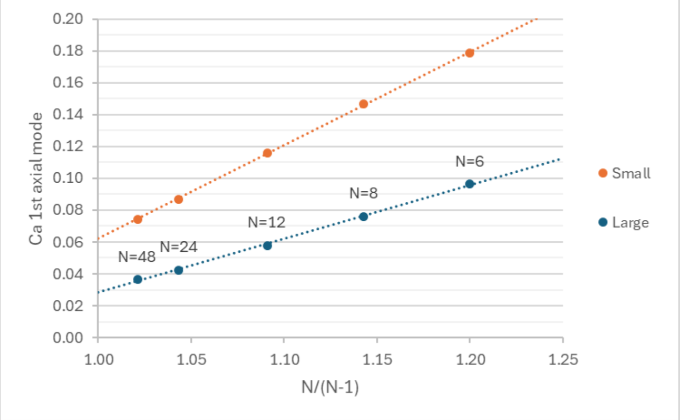

FIGURE 23: ADDED MASS COEFFICIENT FIRST AXIAL MODE

4. BASIN TESTS

4.1 Test setup

To validate the wave frequent surge response and axial connector load, seakeeping tests were performed in MARIN's Concept basin. Four arrays were tested, namely 6 Small, 12 Small, 6 Large and 12 Large. The test setup for *'12 Large'* is shown in Figure 26. A horizontal soft mooring system was specifically designed for the tests, with all fairleads at the most waveward pontoon. In this way the mooring system does not induce loading in the connectors. Offshore, practically this can be hardly avoided. However, for the purpose of the tests the mooring induced connector load was deliberately excluded. The stiffness of the mooring lines was chosen so that the natural frequency of the moored system is one order of magnitude longer than the longest wave frequency tested.

The arrays were instrumented with a motion tracking target on the most waveward pontoon (Figure 24) and a connector load force measurement (Figure 25). The connector load was measured at the central hinge, i.e. in-between pontoons 3 & 4 for the arrays consisting of 6 pontoons and in-between pontoons 6 & 7 for the arrays consisting of 12 pontoons. Each array was tested with 6 irregular waves as listed in Table 5.

FIGURE 24: 12 SMALL WITH MOTION TARGET

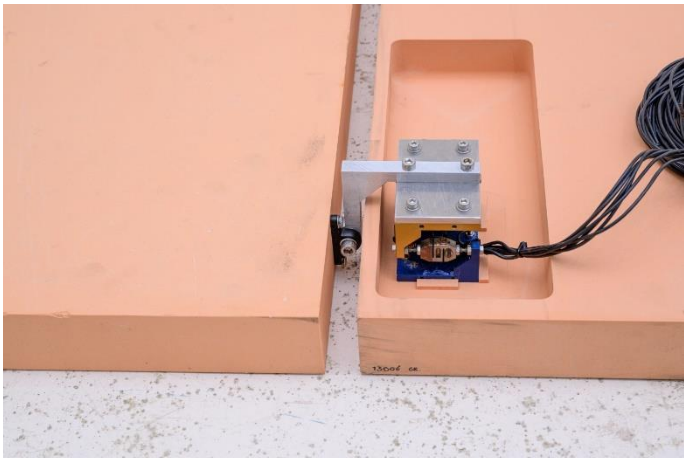

FIGURE 25: CONNECTOR FORCE MEASUREMENT

Table 5: Tested irregular waves

	Hs	Tp	Dir.	γ
	[m]	[s]	[deg]	[-]
Irregular 1	0.018	0.90	180	3.0
Irregular 2	0.036	0.90	180	3.0
Irregular 3	0.036	1.20	180	1.9
Irregular 4	0.072	1.20	180	1.9
Irregular 5	0.036	1.70	180	1.1
Irregular 6	0.072	1.70	180	1.1

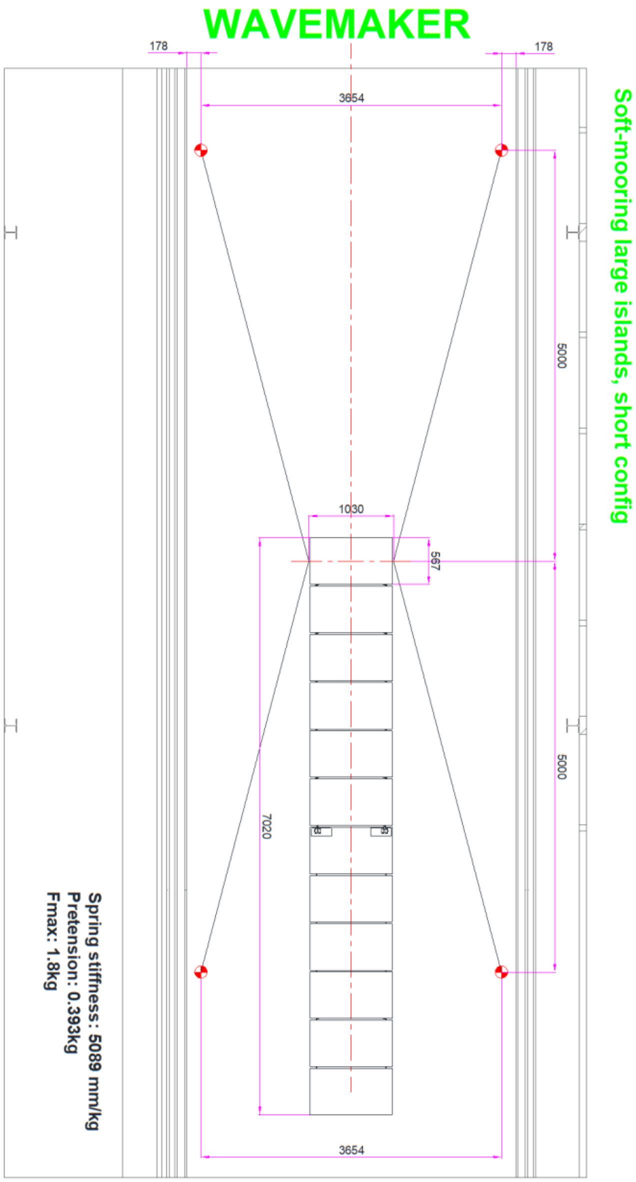

FIGURE 26: 12 LARGE MOORED IN CONCEPT BASIN

4.1 Post-processing

The RAO for motions and hinge loads have been derived for all irregular wave tests using the spectrum method:

$$RAO\ (\omega) = \sqrt{\frac{S_{response}(\omega)}{S_{wave}(\omega)}} \tag{42}$$

As we divide the response by the spectral density of the incoming wave, the RAO can only be determined at those frequencies where $S_{wave} >> 0$. Consequently, the RAO is determined at frequencies where $S_{wave}(\omega) > 0.2\ S_{wave}(\omega_p)$. This 20% threshold is a compromise, selecting a higher threshold will improve the signal to noise ratio, while a lower threshold results in a broader frequency range.

The resulting RAO for the motions and axial loads is shown in Figures 27 and 28 respectively. If a system has a perfectly linear response, in a basin without any random uncertainties, the RAOs of all 6 irregular wave tests are in-line with each other. If two irregular wave tests result in a different RAO, this is due to a combination of non-linearities in the response and because of random uncertainties in the test setup. The plotted mean represents the average value of all irregular wave tests where the wave energy exceeds the threshold.

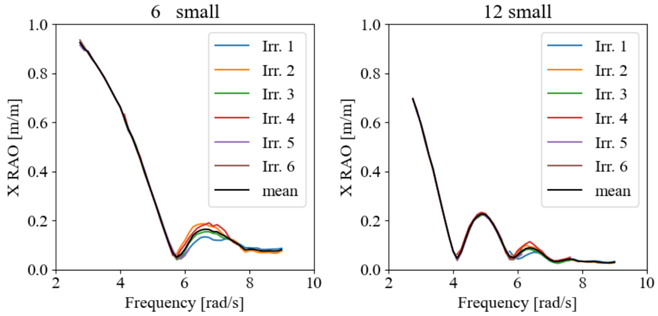

FIGURE 27: MOTION RAO 6 & 12 SMALL

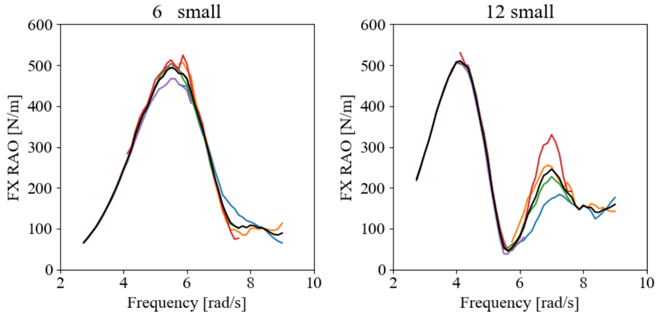

FIGURE 28: AXIAL LOAD RAO 6 & 12 SMALL

4.2 Validation

The mean value resulting from 6 irregular wave tests was compared to the DIFFRAC results and the analytical solution. The results are shown in Figures 29 and 30 and respectively correspond to motions and connector loads. A repeat test was performed for the 12 pontoon system (Small array), where the load sensors were placed to a more waveward position at *X/L* = 0.25 (i.e., between pontoons 3 & 4, see Figure 30). For the motions as well as for the axial loading, results from software DIFFRAC and model tests are in good agreement. The analytical solution is satisfactory especially for the longer arrays. The best agreement is seen for array *'12 Large'*.

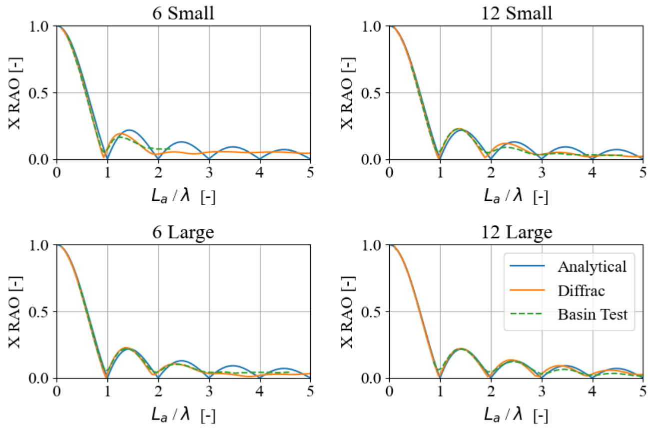

FIGURE 29: VALIDATION HORIZONTAL MOTION RESPONSE

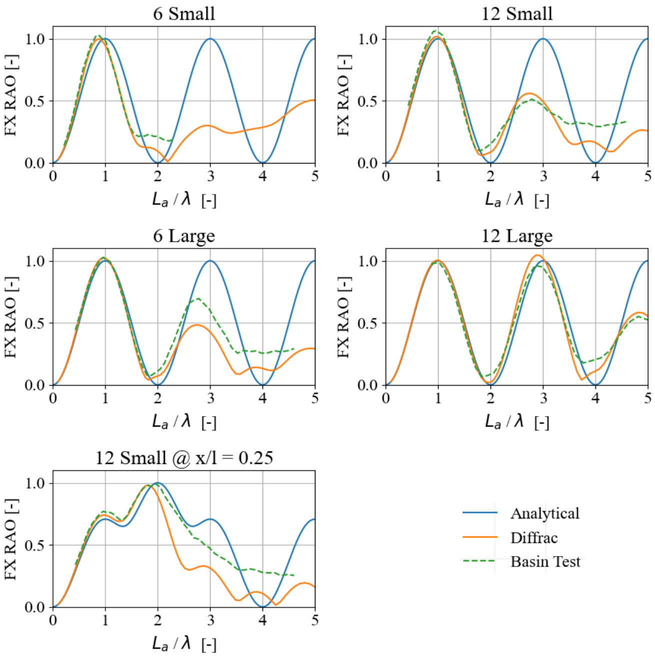

FIGURE 30: VALIDATION AXIAL LOAD RESPONSE

5. CONCLUSION

This paper presented the wave induced responses of shallow draft interconnected pontoons as investigated by the EU-funded project BAMBOO. It is shown that the expansion of the arrays of shallow draft interconnected pontoons reduces the wave frequent horizontal motions. Notwithstanding this, the associated wave frequent axial connector loads do not necessarily amplify as they are mostly related to the stiffness and damping of the system. The analytical solution derived for the axial natural frequencies and axial loading patterns appears to be in good agreement with hydrodynamic diffraction theory and model tests in head waves. The results may be considered important for the development of future classification rules, design assessment procedures and the certification of hybrid wind solar farm installations.

ACKNOWLEDGEMENTS

All authors would like to acknowledge funding from European CINEA under project BAMBOO (Grant Agreement Number : 101136142) . The views and opinions expressed in this paper arethose of the authors and do not necessarily reflect the opinions of CINEA or their respective organizations.

Funded by the
European Union

REFERENCES

[1] IEA (2024), *World Energy Outlook 2024*, IEA, Paris https://www.iea.org/reports/world-energy-outlook-2024, Licence: CC BY 4.0 (report); CC BY NC SA 4.0 (Annex A)

[2] IEA (2022), *Is the European Union on track to meet its REPowerEU goals?*, IEA, Paris https://www.iea.org/reports/is-the-european-union-on-track-to-meet-its-repowereu-goals, Licence: CC BY 4.0

[3] Soppe, W.J., Jong, M.M. de, Huisman, M., Folkerts, W.,Kroon, J. *Challenges and potential for offshore floating solar in the Dutch North Sea*, 40th European Photovoltaic Solar Energy Conference and Exhibition, Lisbon, Portugal

[4] Airy, G., 1845. *Tides and waves*. London, pp. 241–396

[5] Journée J., Massie W. *Offshore Hydrodynamics*, Delft University of Technology 2001

[6] Rao S., *Mechanical Vibrations*, ISBN 978013048987

[7] Lamb, H. (1932). Hydrodynamics. *Dover Publications, Inc., New York,*

[8] Bunnik T., Pauw W., Voogt A. *Hydrodynamic analysis for side-by-side offloading*, ISOPE 2009